sciendo Studia Geotechnica et Mechanica, 2024; 46(2): 77–90

Original Study **Open Access**

Jonathan Marliot*, Stephen Hedan, Marja Siitari-Kauppi, Juuso Sammaljärvi Catherine Landesman, Pierre Henocq, Paul Sardini

Comparing fracture openings in mortar using different imaging techniques

https://doi.org/10.2478/sgem-2024-0004
received December 15, 2023; accepted February 23, 2024.

Abstract: This paper presents a quantitative characterisation of the fracture openings obtained in triaxial shear tests on several cement mortar samples. The comparison was carried out on three samples with various apertures using different methods of semi-destructive and non-destructive characterisation: optical microscopy, scanning electron microscopy, X-ray computed tomography, digital volume correlation and the ^{14}C-polymethylmethacrylate method. The fracture aperture distribution results are in good agreement between the different methods. Although the opening results obtained are comparable, the most advantageous method was considered to be XRCT profile analysis based on the size of the target area studied and the specific characteristics of each technique.

Keywords: mortar; fracture apertures; characterisation method; process duration; disadvantages.

1 Introduction

For both surface and underground radioactive waste repositories, cement-based materials (mainly concrete) are currently used or foreseen as (i) barrier against radionuclide migration towards the biosphere, (ii) conditioning matrices and (iii) vault structure [1]. Concrete, in particular, has advantageous properties in terms of solute transport due to its low permeability [2, 3]. However, the behaviour of these materials may be subject to medium- or long-term alterations due to the effect of mechanical and chemical stresses. Fractures, which are generated by these mechanical deformations, would constitute major pathways for the radionuclide transport through the cementitious barrier.

In this context, it is crucial to accurately characterise the geometry of the fractures, mainly by knowing their aperture and density. This knowledge is necessary to better understand their role in the migration of radionuclides through cement-based materials.

Characterisations of fracture geometry in previous studies have been generally done using only one, two or three different characterisation methods [4, 5, 6, 7, 8], especially among optical microscopy (OM), scanning electron microscopy (SEM) [9], X-ray computed tomography (XRCT) [10], digital volume correlation (called H-DVC) [11] and the ^{14}C-polymethylmethacrylate (^{14}C-PMMA) method [12], and rarely on the same material. Optical and electronic microscopies were used to estimate aperture distribution using manual measurements taken at random points. These two methods enable the average aperture to be known but are not adequate to obtain a distribution [9]. The development of XRCT over more than two decades has enabled the 3D architecture of the pore space to be mapped [8, 10]. Nowadays, fractures are almost routinely characterised by using XRCT [13]. This non-destructive technique is well-suited for quantitatively mapping the aperture distribution and the fracture density [13]. In this study, a new algorithm for aperture estimation based on the analysis of grey-level profiles is presented and tested. A second modality of this method is H-DVC, which is based on the comparison between the volumes recorded before and after fracturing [14, 15]. Using H-DVC, new advances in fracture characterisation methods are presented. Finally, the ^{14}C-PMMA method has previously been applied for extracting the fracture apertures from autoradiographs [12, 16]. This method has been recently extended to deducing fracture apertures from 2D activity maps (A/A_0) [16] and porosity maps [17].

***Corresponding author: Jonathan Marliot,** Poitiers University, CNRS, IC2MP, UMR 7285 – Poitiers, France, E-mail: jonathan.marliot@univ-poitiers.fr
Stephen Hedan, Paul Sardini, Poitiers University, CNRS, IC2MP, UMR 7285 – Poitiers, France
Marja Siitari-Kauppi, Juuso Sammaljärvi, Radiochemistry, Department of Chemistry, Helsinki University – Helsinki, Finland
Catherine Landesman, Subatech laboratory, UMR 6457, CNRS/IN2P3, IMT Atlantique, Nantes University – Nantes, France
Pierre Henocq, French National Agency for Radioactive Waste Management (Andra) – Châtenay-Malabry, France

The aim of this study is to compare the characterisation of fracture networks (apertures and density) in three artificially fractured cement-based samples. The studied fractures were generated in the laboratory using a triaxial press, and the results obtained by these methods are compared in terms of aperture distribution. All the methods mentioned above were used on all the samples except the H-DVC technique which was performed only on one sample.

2 Materials and methods

2.1 Preparation of undamaged mortar

In the present work, mortar was used instead of concrete, even if it would have been more realistic to use concrete, since it is the primary cementitious material employed in nuclear waste storage facilities. However, in terms of representative elemental volume (REV), it would have been necessary to create and fracture fairly large cores (several tens of centimetres) due to the size of the gravel grains in the concrete. Instead, mortar an analogue material to concrete permitted smaller samples (a few centimetres) thanks to its medium grain size and was, therefore, easier to adapt to the various imaging techniques. In addition, the use of concrete would have led to problems when fracturing the material, as a larger sample would have required the use of a higher stress to achieve material failure, an increase that would not have been feasible with the equipment available. In addition, a large sample size also involves coring the material to obtain moderately sized samples for performing radionuclide (RN) transport experiments (through-diffusion experiments); this coring could have resulted in fracture-widening or material destruction.

The cylindrical mortar samples for this study were casted with a water/cement = 0.5 and sand/cement = 3.2, with standardised silica sand 0-4 mm CEN EN 196-1 (“Société Nouvelle du Littoral”), milliQ water (Ultra-pure (18 MΩcm)) and CEM I cement (Val d’Azergues 52.5R, LafargeHolcim Ciments).

The mixing protocol used for the mortar was as follows:

- Mix cement and sand at 30 rpm for 3 min.
- Add the water, mixing at 30 rpm for 30 sec.
- Mix at 90 rpm for 3 min.
- Fill the moulds tier by tier, vibrating after each fill (diameter 35 mm, height 65 mm).

Different vibration methods were tested to reduce the size and number of air bubbles, including 15 sec for tiers 1 and 2, and 1 min 15 sec for tier 3 versus 1 min 15 sec per tier, with the aim of decreasing the structural fragility of the material during fracturing.

Analysis of the air bubbles by thresholding was conducted using Fiji software on the XRCT images, as shown in Figure 1. The percentage of pixels detected inside the bubbles was normalised by the number of pixels corresponding to the mortar cylinder, to determine the percentage of bubble porosity.

By comparing the bubble porosity in the study area, where the samples for the RN transport experiments came from, its percentage decreased from an average of 3.5% ± 1.2% for (A) to 1.9% ± 0.4% for (B); the diameter of these bubbles also varied from 1.7–2.7 mm for (A) to 1.3–1.7 mm for (B). Beyond the study area, the characteristics of the bubble porosity approached and eventually became the same for both methods (A) and (B).

The mortar cylinders were left to harden for 24 hours and were then removed from the mould and left to cure for at least one month in calcium hydroxide-oversaturated water. The maturation was monitored by tracking the mass of the samples, and after a few weeks, the masses began to stabilise.

2.2 Mechanical damaging of mortar

After the maturation period, the mortar cylinders were induced to fracture using the triaxial shear test apparatus. First, the confining pressure (σ_3) was increased until 0.8 MPa. Then, using a motor set at a speed of 0.15 mm/min, the axial pressure (σ_1) was increased to cause the material to fracture. The increase of σ_1 was controlled by a force sensor connected to a monitor. The main challenge of this experiment was to obtain mortar cylinders presenting micro-fractures, observable by XRCT, but with the samples still remaining cohesive.

To achieve this, the force sensor was essential for monitoring during the whole triaxial test: the force values rose gradually during the test and began to stabilise when the failure zone was reached. At this step, the experiment was stopped, and the deviatoric stress was recorded q (with $\sigma_1 = \sigma_3 + q$). The mortar sample was subsequently removed from the press, and plastic clamp rings were carefully installed around it to ensure that the material remained intact for the later analyses.

For all fractured mortars, the success of the triaxial shear tests was quite low: for the 15 tests carried out,

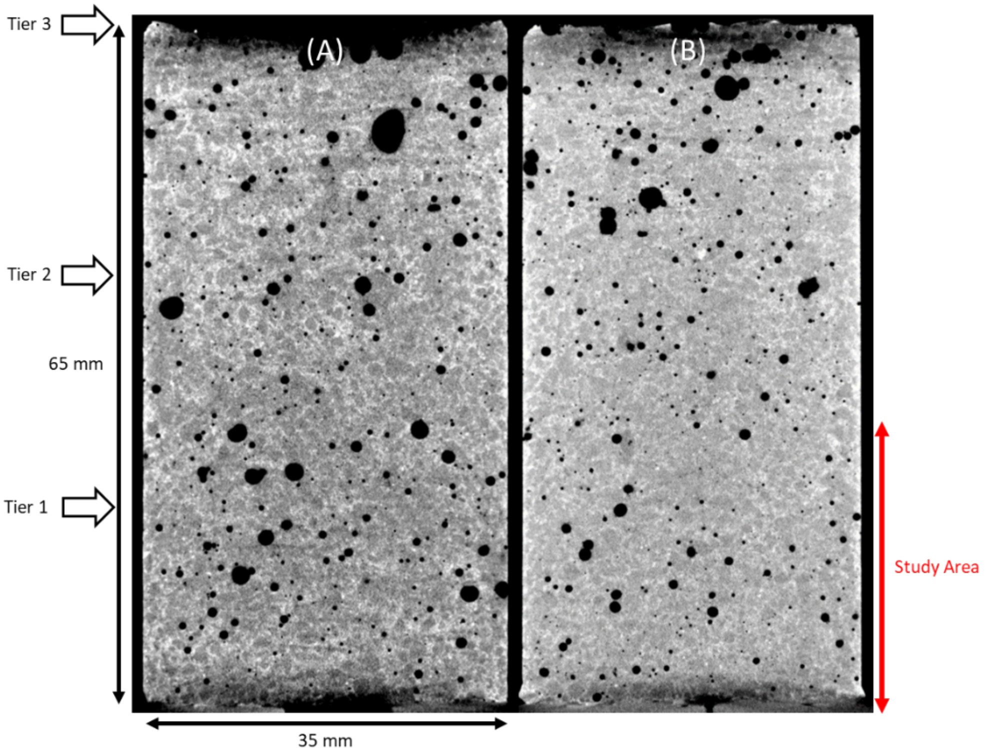

Figure 1: Comparison of two mortar samples' XRCT images obtained from different vibration methods: 15 sec for tiers 1 and 2 and 1 min 15 sec for tier 3 (A) versus 1 min 15 sec per tier (B).

only 36% of them where fractured in a way that created fractures parallel to the σ_1 visible by XRCT and yet avoided the samples being completely broken (43% of the mortars samples were completely fragmented, while 21% had no visible fracture, using XRCT). Considering the samples for which the test was successful, the maximal principal major stress σ_1 used to reach the point of fracture varied from 31 to 38 MPa.

2.3 Preliminary characterisation of the material

The undamaged saturated samples were characterised by analysing their water porosity and water permeability. For the fractured samples, only their water permeability values were tested at the IC_2MP laboratory (Poitiers University, France) using cylindrical samples 3.5 cm in diameter and less than 2 cm in thickness.

The bulk connected porosity of the undamaged samples was evaluated using the triple-weighting method. The samples were first dried in an oven at 60°C or 105°C, and their dry mass was measured (M_{dry}). Then, the samples were placed under a bell jar and subjected to vacuum. The water level was then increased very slowly to achieve optimum saturation of the material by expelling the air contained in the material's porosity. This increase in the water level was carried out over one week until the samples were fully immersed, after which the samples were left immersed for two to three weeks. The samples were then removed from the water, and their saturated mass (M_{sat}) and the saturated mass suspended in the water (M_{susp}) were taken in order to calculate a porosity value (ϕ) using Eq. (1). Finally, it was found that the average sample porosity was quite different depending on the drying protocol: 11.9% ± 2.2% for drying at 60°C and 17.4% ± 1.3% for drying at 105°C.

$$\Phi = \frac{(M_{sat} - M_{dry})}{(M_{sat} - M_{susp})} * 100 \qquad (1)$$

The water permeability of the mortar samples was measured in the steady-state mode. The investigated samples were left to dry for 24 hours in an oven at 60°C before being epoxy resin-coated in a metal mould created for the purpose. After 48 hours, the resin hardened, and then the resin-coated sample was removed from the mould, and the resin was cut and polished to obtain parallel surfaces. The sample was then left for between 2 and 4 weeks in water to saturate the mortar, and then the sample was placed in a cell for measuring water permeability under a steady-state flow [18, 19]. A pressure differential (ΔP) was established between the upstream and downstream reservoirs of 2 bars for the undamaged materials and of 0.9 bar for the fractured mortars. For a low-permeability material such as undamaged mortar, a minimum of one week was needed to reach a steady-flow state. Using Darcy's law (Eq. (2)), an average permeability value for the undamaged mortar was measured at $1.3 \pm 1.6 \times 10^{-19}$ m² [20] with a measured flow rate of $1.0 \pm 1.4 \times 10^{-12}$ $m^3.s^{-1}$. For the fractured materials, the permeability value depended on fracturing, and for the samples studied, it was approximately $1.5 \pm 2.0 \times 10^{-16}$ m² with a measured flow rate of $5.0 \pm 5.0 \times 10^{-9}$ $m^3.s^{-1}$.

$$k = \frac{(Q * \mu * L)}{(S * (\Delta P * 10^5))} \tag{2}$$

k: intrinsic permeability (m²); Q: measured flow rate ($m^3.s^{-1}$); μ: dynamic viscosity of water (Pa.s): 1.0×10^{-3} Pa.s; L: sample thickness (m); S: sample surface area (m²): 1.26×10^{-3} m²; ΔP: pressure difference (bar).

2.4 Methods for fracture aperture analysis

In this study, triaxial shear tests using a low confining pressure produced one or several fractures parallel to the σ_1 main stress axis. The fracture apertures observed and measured in these sections are considered to represent real apertures since the observation plane (XZ) is perpendicular to the fracture plane(s). Among all suitable fractured samples, three of them were selected for estimating fracture apertures (#5, #39 and #16 in ascending order of fracture width). These three samples were chosen to be presented here because of their contrasted aperture distribution. The first two techniques described below are optical microscopy (OM) and scanning electron microscopy (SEM); both are semi-quantitative techniques involving manual measurements taken at random points. The other techniques used were X-ray computed tomography (XRCT), heaviside-digital volumetric correlation (H-DVC) and ^{14}C-polymethylmethacrylate (^{14}C-PMMA): these three methods are quantitative techniques using automatic measurements. The employed algorithms are described below.

2.4.1 Optical microscopy

The optical microscope used was a NIKON Eclipse E600 POL equipped with a camera (T-TV 55 NIKON JAPAN). Using reflected light, it was possible to observe the minerals and fractures affecting the samples which were several millimetres thick. With polarised light, it was difficult to detect the impregnated fractures. To observe the fractures more easily, this method required the use of non-polarised light, and the dark-coloured fractures are more visible than the sand grains and the whitish-coloured cement matrix (Figure 2(A)).

The distribution of fracture apertures was determined at a number of observation points on the three studied samples: #5: 12 points, #39: 80 points and #16: 33 points. However, it was impossible to assess the density of the fractures using transect methods because of the difficulty of following the continuity of the fractures.

2.4.2 Scanning Electron Microscopy (SEM)

Scanning electron microscopy (SEM) is a technique capable of producing high-resolution images of the surface of a sample using the principle of electron-matter interactions. The device used at Poitiers University is a conventional SEM JEOL JSM IT 500 (LowVacuum) equipped with an energy-dispersion spectroscopy (EDS) detector used for the semi-quantitative chemical analysis of minerals. The settings used were as follows:

- For samples #5 and #39: accelerating voltage: 15 kV, working distance: 10.5 mm, carbon-coated polished section, probe current: 1 nA, magnification: x45 and x95, pixel size: 0.53 µm
- For sample #16: accelerating voltage: 15 kV, working distance: 16.2 mm, carbon-coated polished section, probe current: 1 nA, magnification: x36, pixel size: 2.7 µm

To best observe the fractures, we used the backscattered electron imaging mode (BSEi). The quantity of backscattered electrons collected in the two-diode detector depended on the average Z of the material they encountered (cement matrix, sand grains or PMMA resin) [9, 21]. Using the BSEi mode, the fractures (PMMA resin-filled) appeared in black, contrasted well with the rest of the mortar which was observed as light grey (Figure 2(B)). Thus, the fracture aperture was easy to estimate using this observation mode thanks to the high resolution of the images obtained.

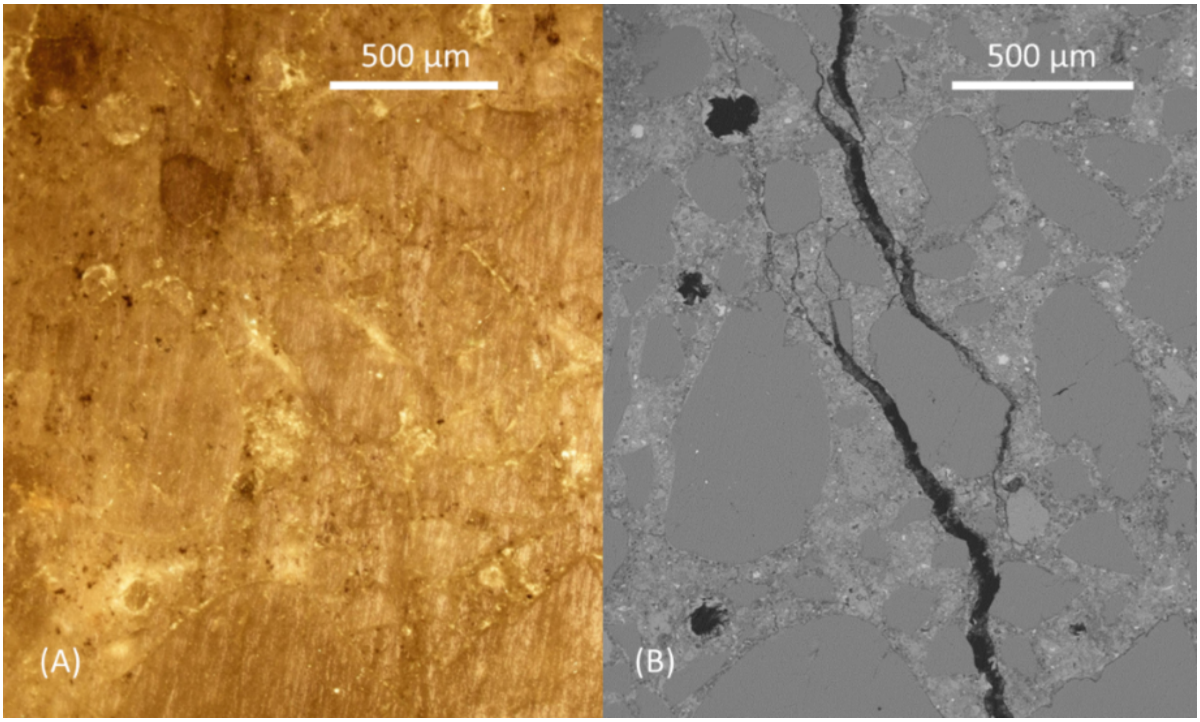

Figure 2: The same area of the fracture in sample #39 visualised by optical microscopy (OM), magnification: x40 (A) and scanning electron microscopy (SEM) using the BSEi observation mode, magnification: x45 (B).

The distribution of fracture apertures was determined by taking many observation points from the studied samples: #5: 59 points, #39: 121 points and #16: 137 points.

2.4.3 X-Ray Computed Tomography (XRCT)

2.4.3.1 Imaging parameters

XRCT enables the non-destructive visualisation of a material's internal structures. It involves passing X-rays through a material to observe its internal structure according to a combination of radiographs [8, 10]. The obtained reconstructed 3D image is in a greyscale, where the grey-level intensity of a given voxel is proportional to the average X-ray attenuation coefficient of the medium contained in this voxel. The voids appear with low-intensity values, and the densest minerals appear with high-intensity values.

The mortar cylinders were analysed by XRCT (Figure 3) (RX Solutions EasytomXL Duo, IC_2MP, Poitiers, France) using the following settings:

- For sample #5: total duration of the scan: 15 minutes, voxel size: 54.6 µm, X-ray intensity: 270 µA, voltage: 90kV, number of radiographs: 800 images. The XRCT was performed before and after fracturing.
- For samples #16 and #39: total duration of the scan: 1 hour, voxel size: 24.4 µm, X-ray intensity: 220 µA, voltage: 90kV, number of radiographs: 1440 images. The XRCT was performed only after fracturing.

According to the study [8], the minimum aperture size observable by XRCT is approximately a tenth of the voxel size, so about 5 to 2 µm in this study. The analysis procedure was different between sample #5 and samples #39 and #16. The analysis was carried out on the whole mortar cylinder for sample #5 (6.5 cm of height) to obtain an overview, while it focused only on a height of 2 cm for the two other samples, #39 and #16, in order to obtain a better resolution. The X-ray attenuation coefficients were equivalent for samples #5 and #16. Because sample #39 was pre-impregnated with ^{14}C-PMMA, the attenuation coefficient of pores in this sample was greater than that of the two others samples. For instance, when in a voxel there is a mixture solid + air, its attenuation coefficient is lower than a mixture solid + resin. This was why the slice for the resin containing sample was clearer. However, this difference did not pose a problem for the analysis of fracture openings. It should also be noted that for sample #39, the analysis of fracture openings was carried out on the through fracture and not on the fractures at

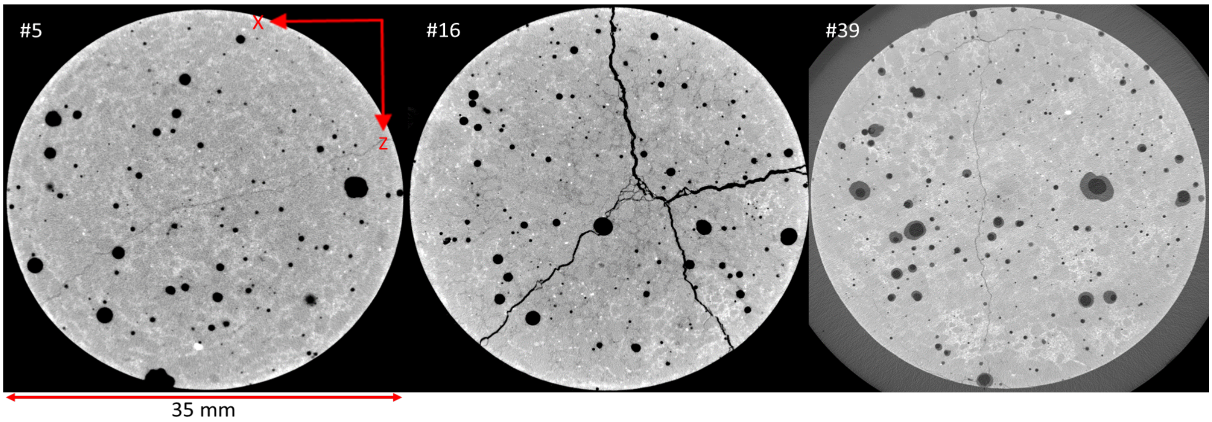

Figure 3: Tomographic slice of samples #5, #16 and #39.

the periphery of the sample, the latter resulting from subsequent damage during sample preparation.

2.4.3.2 XRCT image processing of damaged mortars

An analysis of the fracture openings was carried out on 8-bit grey-level (GL) slices which were perpendicular to the fracture planes. To estimate the fractures' apertures (and densities), it was first necessary to segment them. Segmentation was performed using a combination of classical mathematical morphology tools [22] and Fiji software [23, 24]. The aim of that first step was to obtain the skeleton (or medial axis) of all the fractures. The workflow employed for fracture segmentation is described in Figure 4. In Figure 4c), a mask is generated by a simple thresholding by boundaries, including the fracture and air bubbles. The use of 2D morphological reconstructions and image filtering allows to remove thresholded artefacts and structures which are not connected to the fracture (Figure 4d)), which is furthermore skeletonised using the Fiji command Skeletonize (Figure 4e)). Grey-level profiles perpendicular to the skeleton are generated with a homemade macro command (for ease of viewing, only one of the two profiles are displayed in Figure 4g).

At a first glance, the minimum grey level in a fracture (located on its medial axis) could have been used for estimating its aperture, as this GL comes from the local mixing between the fracture void and the porous matrix. However, this approach is not satisfactory because if a fracture had an opening larger than the voxel size, the grey level on the median axis of the fracture would reach a plateau (a constant value close to the grey level of the PMMA resin GL_r), and the opening would vary independently of the GL on the median axis. In such a case, the aperture would have to incorporate a wider zone around the median axis. An approach incorporating all possible openings was tested by determining the GL profile perpendicular to any point on the fracture skeleton (Figure 4g)). The function GetProfile() implemented as a built-in function within Fiji quickly allows any profile between two points to be obtained (a line thickness of 1 was used for the profile calculations). This function uses a bilinear interpolation to estimate the GL along a line of any orientation. The length of the profile was chosen to be higher than the maximum-expected fracture aperture. Each point i of a profile was converted into a fracture porosity ϕf_i using a MatLab script. For that, it was stated that the grey level GL_i of each point of the profile results from a weighted average between the GL of the pure PMMA resin GL_r and the GL of the porous matrix GL_m, Eq. (3):

$$GL_i = GL_r * \phi f_i + GL_m * (1 - \phi f_i) \tag{3}$$

The fracture porosity ϕf_i term is equal to the “fracture content” in the point i. GL_m was determined with an average value calculated from both ends of the profile. The lowest grey level of the sample caught in large air bubbles (or in some wider fractures) determined GL_r. The fracture porosity ϕf_i is, thus, deduced from Eq. (3) using Eq. (4):

$$\phi f_i = \frac{(GL_m - GL_i)}{(GL_m - GL_r)} \tag{4}$$

With Eq. (4), each fracture porosity value of the profile was transformed into an aperture value using the pixel size (L_p). This aperture was cumulated along the whole

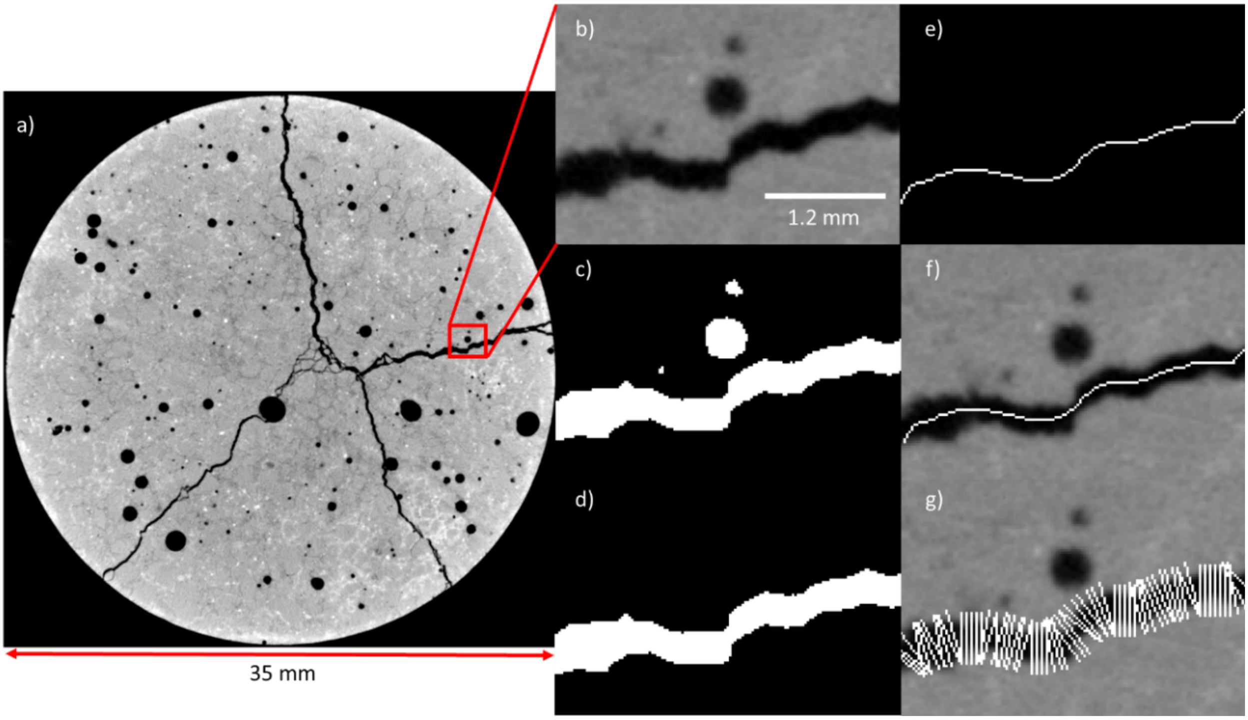

Figure 4: Workflow employed for fracture segmentation. a) Greyscale tomographic slice of sample #16. b) Magnification of a region of interest of a). c) Mask image obtained by thresholding by boundaries, which is filtered in d) to remove structures which are not connected to the fracture. e) Skeletonised fracture. f) Checking the centre of the skeleton in relation to the fracture. g) View of grey-level profiles associated to the skeleton.

profile, Eq. (5), in order to provide the total aperture of the fracture (ω) at the profile position:

$$\omega = \sum \phi f_i * L_p \tag{5}$$

The advantages of this method are first that an aperture value can be obtained with a simple algorithm and second that the position of the medial axis does not necessarily have to correspond to the profile minimum, as the algorithm detects and integrates the minimum grey level (and therefore the maximum porosity) into the sum of the porosity profile. If the calculation had been based on the skeleton point alone, the slightest misalignment between the skeleton and the minimum could have decreased the estimated porosity value. Finally, the last advantage of this method is that the fracture aperture can be determined independently of the voxel size (i.e., it estimates fracture apertures which are higher or lower than the voxel size). This original method was designed for porous media where fracture apertures can be highly variable. The distribution of fracture apertures was determined on a large number of observation points (profiles) for the three studied samples: #5: 693 points, #39: 1602 points and #16: 3773 points.

2.4.4 Digital Volume Correlation (H-DVC)

Digital volumetric correlation (DVC) was applied only on sample #5's XRCT images obtained at two stages: before fracture (C1) and after fracture (C2). As the sample presents a fracture, the eXtended-Digital Volume Correlation (X-DVC, [25]) method was chosen. H-DVC is an extension of DVC for volume analysis and is a non-destructive 3D analysis method derived from eXtended-Digital Image Correlation (X-DIC, [26]) to take the fracture into account. The basic principles of H-DVC have been defined in previous work [25].

The volume used, corresponding to a small slice of the acquired total volumes, was made from 757x69x670 voxels with a calculation of grid of 1x1x1 given. All calculations were made using the H-DVC algorithm with a 3D subset equal to 50x50x50 voxels (2.73x2.73x2.73 mm^3) according to a local contrast. In each data, three components of displacements (u, v, w) were obtained and six independent components of strains were calculated using finite differences of displacement fields [27]. Like H-DVC was used, the new component of jumps (u', v', w'), corresponding to a cutting of the 3D subset into two 3D sub-subsets, separated by a plane, were obtained [25]. All 3D subsets were enriched, and u', v' and w' approach zero when there is no fracture in the 3D subset.

From the local orientation of the plane and the measured vector jump in the 3D subset, the parameters o, s_1 and s_2 were calculated in each datum in a coordinate system of the plane, and their numerical values correspond to the local opening displacement and the local sliding displacements of this plane, respectively [28].

In Figure 5C, the normal strain (Ɛzz) is presented and the results show the strains concentrated into zones or bands which evolved into a fracture. This fracture crosses the sample and confirms the fracture localisation on the X-ray volume taken after the shear test (C2).

For sample #5, the distribution of fracture openings was determined based on a total of 741 observation points taken along the fracture in the three slices around the 2D section analysed by the other methods, and each slice was separated by the voxel size (54.6 µm).

2.4.5 ^{14}C-polymethylmethacrylate (^{14}C-PMMA) method

The ^{14}C-PMMA method is a nuclear-imaging technique allowing the quantitative mapping of the porosity of porous geo-materials [8, 12, 16, 29, 30, 31, 32]. In the present work, the ^{14}C-PMMA method was applied at the POSINAM facilities at the IC$_2$MP laboratory in Poitiers. The method involved firstly the total impregnation of the mortar samples with methylmethacrylate (^{14}C-MMA), a liquid monomer doped with the radionuclide carbon-14 which is a beta emitter. The samples were then inserted into a polypropylene (PP) container which was placed in an impregnation cell under vacuum. ^{14}C-MMA was mixed with benzoyl peroxide (BPO), a chemical initiator allowing thermal polymerisation of MMA, before impregnating the sample. The ^{14}C-MMA activity used for mortar impregnation was A_0 = 92.5 MBq/L. The mortar samples were left to impregnate for 3 months for sample #5, 1 month for sample #39 and 2 weeks for sample #16.

After the impregnation period, the sample was placed in a water bath (Huber Pilot ONE) to polymerise the MMA into PMMA (polymethyl methacrylate). The temperature programme used imposed a slow temperature ramp from 30°C to 50°C over four days, followed by a plateau at 50°C. Once polymerisation was complete (5–6 days), the sample was removed from the container, which was subsequently cut and polished in preparation for the autoradiography.

Autoradiography captures the decay of ^{14}C beta-emitter electrons by exposing a sample's polished surface on a photographic film (Kodak BioMax MR-1 Film, 18x20) in darkness for about four days. The exposure allows the film to accumulate and record the flashes of electrons from the radioactive decay of ^{14}C. A set of ^{14}C-PMMA standards were also exposed with the samples in order to correlate the film's grey levels to the activities [12]. The film was finally digitised using a table scanner (ArtixScan F1, Microtek), with the following parameters: an 8-bit greyscale image and a 2400 dpi resolution (pixel size is 10.6 µm). Then, the digitised film was processed using Fiji software [23, 24] in order to transform the grey level of each pixel of the film to a nominal activity A/A_0 or to a porosity (for sample #16). Please consult the existing literature providing more explanation of this calculation step [29, 33].

The apertures of fractures in samples #5 and #39 were estimated from the A/A_0 images using the method proposed by [16]. The fractures were first skeletonised with the same procedure used for the XRCT images. Secondly, the profiles perpendicular to each point of the skeleton were obtained, and the maximum of A/A_0 in each profile was determined. These maximum nominal activities were multiplied by a factor called i_R as used in ref [16], allowing A/A_0 to be transformed into an aperture. We used i_R = 80 µm as proposed in refs [16, 17]. Note that the present methodology is more versatile than using watershed for determining the maximum activity on the fracture skeleton.

To analyse the fracture opening of sample #16, another treatment was carried out, using the porosity image. The fractures were first skeletonised using the same procedure as for the XRCT images. Profiles perpendicular to each point of the skeleton were generated, and the porosity of each point of the profile was recalculated by subtracting the value of the matrix, except when the porosity value was 1. These values were then multiplied by the pixel size (10.6 µm) and summed to obtain an aperture value for each profile. This approach differs from that of [16], and the results obtained are discussed below (section 3.2.).

The distribution of fracture apertures was determined by taking many points from the samples (#5: 3553 points, #39: 3425 points and #16: 7116 points).

Table 1: Summary of average fracture opening obtained using microscopy methods: optical microscopy (OM) and scanning electron microscopy (SEM). The number of observation points is indicated in brackets.

	#5 (μm)	#39 (μm)	#16 (μm)
OM	15.6 ± 5.5 [12]	29.3 ± 14.6 [80]	131.8 ± 85.7 [33]
SEM	15.8 ± 6.1 [59]	25 ± 14.2 [121]	129.5 ± 136.8 [137]

Table 2: Summary of average fracture opening obtained using X-ray computed tomography (XRCT), ^{14}C-PMMA autoradiographs (^{14}C-PMMA) and heaviside-digital volumetric correlation (H-DVC) methods. The numbers of data used to calculate the average values are indicated in brackets.

	#5 (μm)	#39 (μm)	#16 (μm)
XRCT	21.2 ± 9.1 [585]	32.1 ± 13.1 [1549]	120.1 ± 68.3 [3685]
H-DVC	18.6 ± 8.1 [741]	-	-
^{14}C-PMMA	18.6 ± 5.7 [3414]	26.1 ± 8 [3331]	180.2 ± 72.4 [6051]

3 Results

3.1 Results obtained using microscopy methods

The optical microscopy (OM) and scanning electron microscopy (SEM) results were measured at several points on the fractures from a single surface per sample; see Figure 2 for an example. A distribution of the fracture openings was obtained using the measurements taken manually at random points (Table *1*). Although the distribution was derived from a relatively small number of values, the averages obtained from SEM and OM were in fair agreement. For sample #5, ω = 15.6 μm by OM and ω = 15.8 μm by SEM. For sample #39, ω = 29.3 μm by OM and ω = 25 μm for SEM. For sample #16, ω = 131.8 μm for OM and ω = 129.5 μm by SEM.

Using microscopy techniques, it was not possible to obtain a complete map of the fracture network due to the difficulty of tracking fractures using the OM method and the very long time required for the SEM method. However other techniques were used to provide this global mapping much more rapidly.

3.2 Results obtained by 2D/3D mapping methods

The results of the other methods were obtained on the same surfaces as the microscopic methods for ^{14}C-PMMA, the equivalent surface for each sample for the XRCT images and a set of three surfaces around the surface analysed by microscopy for H-DVC, and each was separated by the size of a voxel. In addition, as the analyses were carried out on the complete 2D sections of the samples by XRCT and ^{14}C-PMMA, the distribution obtained is based on many more measurement points than were used by OM and SEM. The distribution of apertures is, therefore, more detailed, and it has been possible (1) to plot the distribution of the apertures and (2) to locate and spatially differentiate sub-zones of whole fractures on the basis of their range of opening.

Although these methods for mapping fracture openings were very different in terms of process duration and calculation, it should be noted that they provide comparable average results (Table 2).

For sample #5 (Figure 5), the average apertures measured by the three techniques are quite close between 18.6 μm by H-DVC and ^{14}C-PMMA and 21.2 μm by XRCT. Average aperture values were obtained without considering apertures greater than 50 μm for the XRCT method, data corresponding to air bubbles (9.8%) and artefacts (5.8%), which are represented by points in Figure 10. These artefacts were generated due to the low resolution of the XRCT images used. For the ^{14}C-PMMA method, the average aperture value was calculated excluding the air bubbles (4%).

For sample #39, the average apertures measured by the XRCT and ^{14}C-PMMA methods, obtained without considering the air bubbles (3.3% for XRCT and 2.7% for ^{14}C-PMMA), are also similar and are about one and a half times wider than the apertures found for sample #5: ω = 32.1 μm (XRCT) and ω = 26.1 μm (^{14}C-PMMA).

Using the different imaging methods, the aperture distributions for samples #5 and #39 are similar (Figure 6, Figure 7). The distributions show fractures having a single mode of aperture for each sample, which is smaller than the pixel size for sample #5 (ω = 20 μm ± 10 μm) and which is slightly larger than the pixel size for sample #39 (ω = 30 μm ± 15 μm).

For sample #16, the obtained average openings are much higher and more dispersed: ω = 120.1 μm using XRCT and ω = 180.2 μm using the ^{14}C-PMMA method. The amount of air bubbles for XRCT (2.3%) and poorly impregnated fracture for ^{14}C-PMMA (15%) could be measured even though they were not visible in Figure 8.

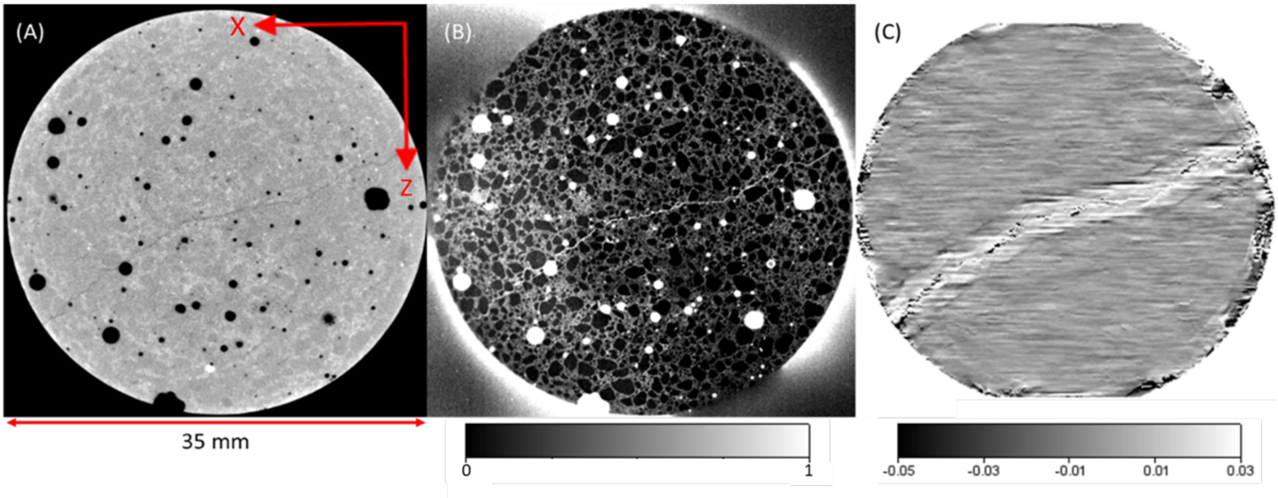

Figure 5: Mapping of the same fractured sample, #5, with X-ray computed tomography (XRCT) (A), A/A_0 mapping obtained from ^{14}C-PMMA autoradiography (B) and the normal strain (Ɛzz) obtained by heaviside-digital volumetric correlation (H-DVC) (C).

Table 3: Comparison of fracture densities calculated using the XRCT and ^{14}C-PMMA methods. These results were obtained from the same data used to calculate the mean aperture values presented in Table 2, except for the ^{14}C-PMMA method for sample #16 where all the data were considered.

	Fracture densities (mm^{-1})	
	XRCT	**^{14}C-PMMA**
#5	3.3 ± 0.3 x 10^{-2}	3.7 ± 0.4 x 10^{-2}
#39	3.8 ± 0.4 x 10^{-2}	3.5 ± 0.4 x 10^{-2}
#16	9.1 ± 0.9 x 10^{-2}	7.6 ± 0.8 x 10^{-2}

These pores were not considered for calculating the average values; therefore, the average value of the ^{14}C-PMMA technique is higher than the average value of the other methods, as observed in Figure 10. The aperture distribution of sample #16 highlights the presence of fractures of different widths: some fractures have an aperture smaller than the pixel size, others are very wide (around 300 µm) (Figure 8). Using the XRCT method, fracture apertures for this sample can be separated into three categories of opening, 35 µm ± 30 µm (red), 120 µm ± 55 µm (orange) and 220 µm ± 50 µm (yellow) and the air bubbles in purple (Figure 9). In addition, as shown in Figure 10, the SEM method was capable of showing bubble sizes exceeding 750 µm, whereas XRCT only gave an estimate of the bubble percentage but not their size, and ^{14}C-PMMA gave maximum bubble sizes of around 350 µm due to the porosity map processing technique used.

Concerning the fracture densities (d_f), values could be obtained from the XRCT and ^{14}C-PMMA methods thanks to

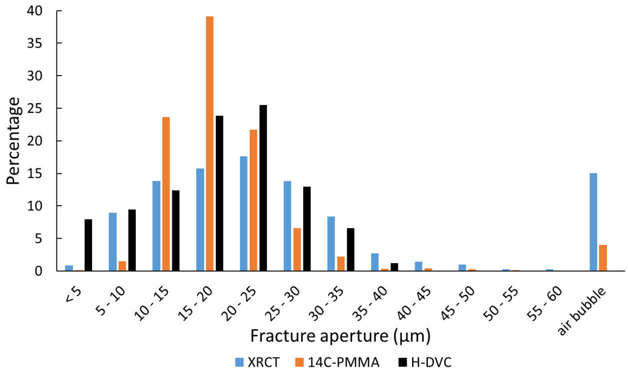

Figure 6: Sample #5: Fracture aperture distribution, XRCT (blue), ^{14}C-PMMA (orange) and H-DVC (black) methods. The distributions are displayed as probability density functions. Voxel size for XRCT and H-DVC methods: 54.6 µm and pixel size for the ^{14}C-PMMA method: 10.6 µm.

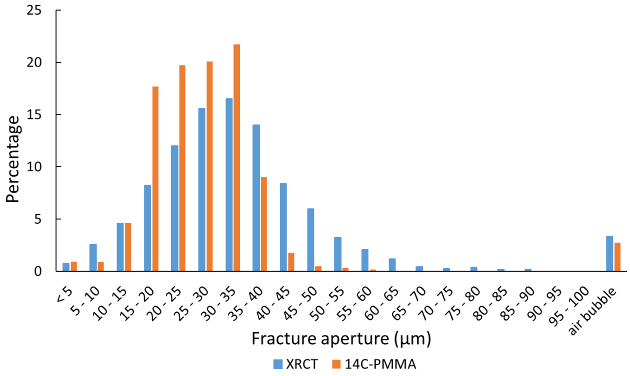

Figure 7: Sample #39: Fracture aperture distribution, XRCT (blue) and ^{14}C-PMMA (orange) methods. The distributions are displayed as probability density functions. Voxel size for the XRCT method: 24.4 µm and pixel size for the ^{14}C-PMMA method: 10.6 µm.

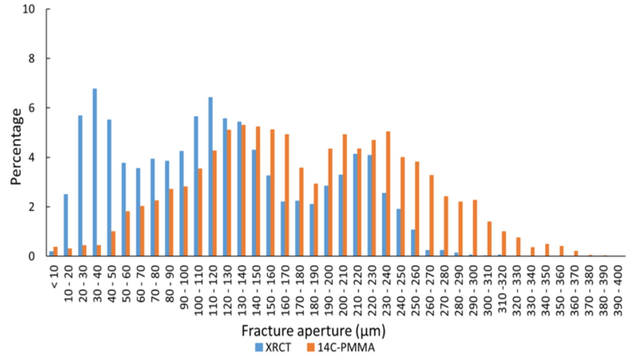

Figure 8: Sample #16: Fracture aperture distribution, XRCT (blue) and ^{14}C-PMMA (orange) methods. The distributions are displayed as probability density functions. Voxel size for the XRCT method: 24.4 µm and pixel size for the ^{14}C-PMMA method: 10.6 µm.

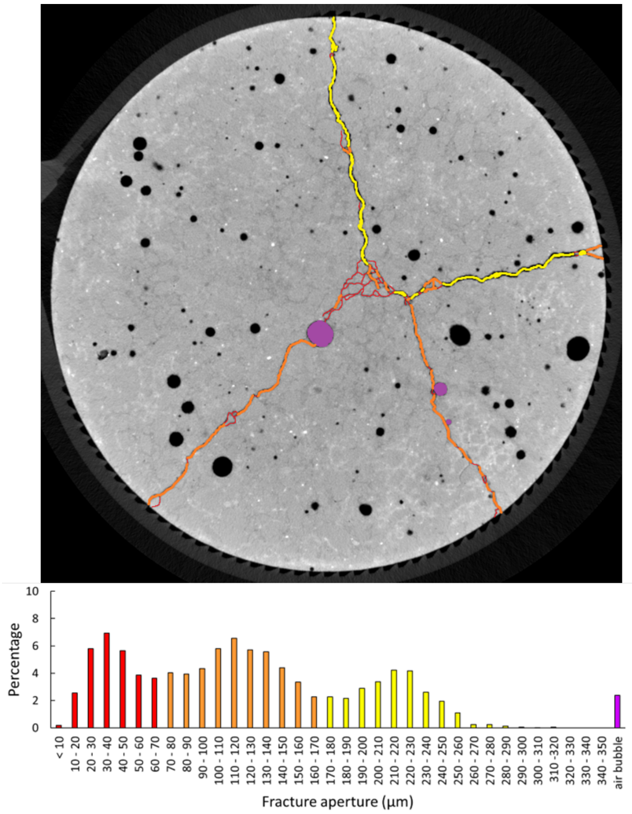

Figure 9: Fracture apertures of sample #16 obtained with XRCT. The distributions are displayed as probability density functions. Voxel size: 24.4 µm.

Eq. (6) using the length of the fracture(s) corresponding to the number of pixels of the fracture skeleton in millimetres (L_f) and the surface area of the section analysed in square millimetres (S_s):

$$d_f = \frac{L_f}{S_s} \tag{6}$$

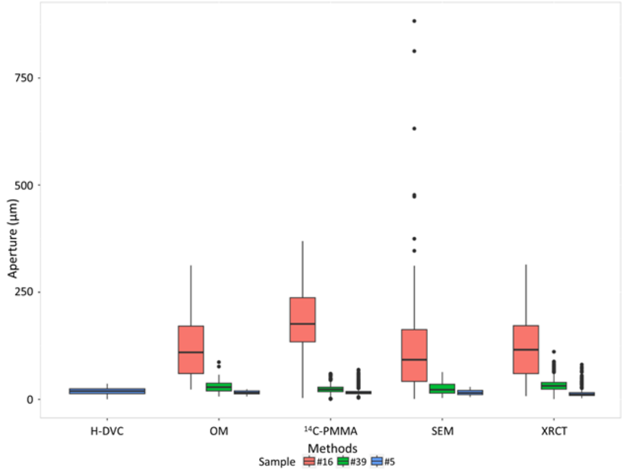

Figure 10: Summary graphic of fracture opening obtained by the five methods. The black dots correspond to the artefact values for the XRCT and ^{14}C-PMMA methods and for air bubbles for the OM and SEM methods.

As shown in Table 3, for samples with a single-fracture-opening category, i.e., #5 and #39 as indicated by their aperture distributions (Figure 6 and Figure 7), the fracture densities are equivalent between the two methods (d_f = 3.6 x 10^{-2} mm^{-1}); although their fracture apertures were different. For a sample with multiple fracture-opening categories, i.e., sample #16 (Figure 9), the density results are higher than for the single-fracture samples, but they remained fairly similar between the two methods (d_f = 8.4 x 10^{-2} mm^{-1}).

4 Discussion/Perspectives

Although the fracture aperture results obtained with all these different analysis techniques give fairly similar results, the process durations and the constraints associated with the methods are totally different.

The microscopy methods, OM and SEM, are fairly quick to perform and provide results that are fairly close to those of the other analysis techniques. These methods are, however, carried out on only a few zones of interest, and it is, therefore, quite difficult to obtain enough data to obtain sufficiently detailed distributions, especially for samples whose aperture varies from a few micrometres to several hundred micrometres. In addition, using optical microscopy, it is very difficult to detect the fracture network in some samples; this could probably be improved by doping the resin with colorant, something to consider for future analyses. Using the SEM analysis, fracture apertures can be measured accurately

Table 4: Process duration and constraints for each method of aperture and density analysis.

	Process duration	Disadvantages
OM	A few hours	Manual analysis of few points / Difficulties of fracture observation
SEM	1 day	Manual analysis of few points / long analysis time
XRCT	1 day	Fracture detection depends on image resolution
H-DVC	A few weeks / months	Fracture detection depends on image resolution / long process and analysis time, two image acquisitions
^{14}C-PMMA	A few months	Use of radioactive tracer / long process time / semi-destructive method

thanks to the contrasts between the resin and the mineral skeleton. However, if a mosaic of images was made using image stitching, the fractures could be mapped at a large scale using a high-resolution image. As a future goal, the methodology of aperture determination using profiles developed herein for XRCT or ^{14}C-PMMA images could be applied to large SEM images to obtain an overall distribution of fracture apertures [34, 35]. However, due to time constraints, these image stitching were not produced. There were also potential problems with intensity changes during acquisition. This problem should, therefore, be studied in more detail. Initially, we preferred to use SEM in a manual quantitative mode.

The methods using 2D/3D mapping (XRCT, H-DVC and ^{14}C-PMMA) give results that are not only equivalent but also very close to the results obtained by microscopy methods. Thanks to the profile analysis method, which is a new and well-suited method for obtaining a rapid quantification of aperture for all types of images (XRCT /H-DVC/^{14}C-PMMA), it is possible to obtain data giving sufficiently detailed distributions to highlight fractures with different apertures, smaller or larger than the pixel size. This is particularly true for the ^{14}C-PMMA method, as the pixel size is even smaller than those of the other two methods. For the XRCT method with a large voxel size, several cases were possible. There were two possible cases: (i) if the fracture had a sufficiently large opening, the algorithm could indeed detect and quantify openings greater than the voxel size. (ii) If the fractures had an opening smaller than the voxel size, the algorithm could also estimate the openings. In both cases, the aperture was determined using Eq. (4) and Eq. (5). A non-detectable fracture was considered in literature studies [36, 37, 38] to have an aperture less than one tenth of the voxel size, under 5 µm for sample #5 and under 2 µm for samples #16 and #39. In addition, the eye could sometimes detect parts of fractures not taken into account by the algorithm because their GL was confused with the GL of the matrix. The algorithm could, therefore, be improved through the use of the deep learning techniques [39].

On the other hand, it should be noted that the H-DVC and ^{14}C-PMMA methods take a long time compared with that of the XRCT technique due to the processing time for the H-DVC method (a few weeks / months) and due to the sample impregnation for the ^{14}C-PMMA method (between 2 weeks and 3 months). Although these durations take an important part of the processing time shown in Table 4, this time did not constitute a continuous work but a waiting period. It corresponded to the time taken from the start of sample preparation to obtaining the fracture opening results and was different for each method. For OM: cutting / polishing / analysis, for SEM: cutting / polishing / carbon coated / analysis, for XRCT: tomography / image processing, for H-DVC: tomography / image processing and for ^{14}C-PMMA: impregnation / cutting / polishing / autoradiography / image processing. Our samples analysed with OM and SEM were all previously impregnated with ^{14}C-MMA, so to know the duration of our experiments, we need to add the impregnation time. In addition, Table 4 also presented the constraints of the different methods employed.

For the ^{14}C-PMMA technique, the treatment of profiles previously developed by [16] was used on samples #5 and #39. This method was designed by modelling the image produced by a ^{14}C-PMMA-filled fracture, which intersects a non-porous matrix. Mortar is, however, a porous matrix, so the method must be adjusted accordingly. The results obtained suggest that this method is nevertheless transposable for a porous matrix with transverse fracture(s). In fact, the openings found by the ^{14}C-PMMA method are within the range of openings determined by the other methods tested, despite the fact that the activity of the matrix can have a significant impact on the activity detected in the medial axis of the fracture. Accordingly, fractures with small openings would be the most affected by the activity of the matrix. Further simulations of the autoradiography process are required to investigate in more detail the effect of matrix porosity on the determination of fracture opening in A/A_0 or porosity images.

The segmentation method which was employed for delineating fractures on the XRCT images uses a combination of thresholding by boundary and 2D morphological reconstructions in 2D slices of the mortar. The main drawback of this method is that the detected fractures have to be connected to the border of the sample in order to be detected, which was always the case for the studied samples. Another option would be to use alternative fracture detection methods such as the use of top-hat filtering as proposed in ref [8].

3D-mapping of a fracture aperture can also be performed on a volume by treating several contiguous 2D slices. This would be interesting in order to visualise the spatial distribution of the aperture in fracture planes and visualise and characterise the main channels controlling transport within it [40]. For H-DVC and XRCT, this mapping can be performed on cylindrical samples acquired in a single tomographic scan. Analysis of the whole sample is, however, more problematic because if the scan is carried out in a single shot, the resolution will be quite low. For better resolution, we used three sub-volumes to reconstruct the whole volume, but using this technique, reconstruction artefacts at the junctions between each sub-volume are generated. For the ^{14}C-PMMA method, it would be possible to carry out a 3D analysis by making numerous slices a few millimetres thick, but this would increase the manpower required, the amount of waste obtained and the risk of breaking the samples during cutting or polishing. This is why, in this work, we have concentrated on 2D distribution and intercomparison between the methods.

5 Conclusions

Compared to previous works that studied fractures in various materials using only one, two or three different characterisation methods, this study makes it possible to compare the results obtained by several methods, i.e. OM, SEM, XRCT, H-DVC and ^{14}C-PMMA, on the same multiphase material with different fracture openings and densities. Considering their process durations and their advantages and disadvantages, XRCT profile analysis appears to be the quickest method to use and the most adaptable to both small and large fractures. However, it should be borne in mind that SEM is still the most accurate imaging method in terms of image resolution. The development of stitching methods could be applied in the future to determine aperture distribution in mosaic SEM images, which would potentially provide more accurate and representative aperture distributions. The average apertures obtained by XRCT analysis are, however, equivalent to the manual SEM measurements. The modelling of the transport of radionuclides in fractured cementitious materials will further be performed with the apertures obtained by XRCT imaging as input data.

References

[1] Drace, Z., Mele, I., Ojovan, M. I., & Rahman, R. A. (2012). An overview of research activities on cementitious materials for radioactive waste management. *MRS Online Proceedings Library (OPL)*, *1475*, imrc11-1475.

[2] Reinhardt, H. E. (2004). *Penetration and permeability of concrete: barriers to organic and contaminating liquids*. CRC Press.

[3] Hall, C., & Hoff, W. D. (2021). *Water transport in brick, stone and concrete*. CRC Press.

[4] Montemagno, C. D., & Pyrak-Nolte, L. J. (1999). Fracture network versus single fractures: measurement of fracture geometry with X-ray tomography. *Physics and Chemistry of the Earth, Part A: Solid Earth and Geodesy*, *24*(7), 575-579.

[5] Matheus, T. C., Kauffman, C. M., Braz, A. K., Mota, C. C., & Gomes, A. S. (2010). Fracture process characterization of fiber-reinforced dental composites evaluated by optical coherence tomography, SEM and optical microscopy. *Brazilian Dental Journal*, *21*, 420-427.

[6] Voorn, M., Exner, U., Barnhoorn, A., Baud, P., & Reuschlé, T. (2015). Porosity, permeability and 3D fracture network characterisation of dolomite reservoir rock samples. *Journal of Petroleum Science and Engineering*, *127*, 270-285.

[7] Li, Z., Liu, D., Cai, Y., Ranjith, P. G., & Yao, Y. (2017). Multi-scale quantitative characterization of 3-D pore-fracture networks in bituminous and anthracite coals using FIB-SEM tomography and X-ray μ-CT. *Fuel*, *209*, 43-53.

[8] Mazurier, A., Sardini, P., Rossi, A. M., Graham, R. C., Hellmuth, K. H., Parneix, J. C., ... & Caner, L. (2016). Development of a fracture network in crystalline rocks during weathering: Study of Bishop Creek chronosequence using X-ray computed tomography and 14C-PMMA impregnation method. *Bulletin*, *128*(9-10), 1423-1438.

[9] Reed, S. J. B. (2005). *Electron microprobe analysis and scanning electron microscopy in geology*. Cambridge university press.

[10] Kak, A. C., & Slaney, M. (2001). *Principles of computerized tomographic imaging*. Society for Industrial and Applied Mathematics.

[11] Chu, T. C., Ranson, W. F., & Sutton, M. A. (1985). Applications of digital-image-correlation techniques to experimental mechanics. *Experimental mechanics*, *25*, 232-244.

[12] Hellmuth, K. H., Siitari-Kauppi, M., & Lindberg, A. (1993). Study of porosity and migration pathways in crystalline rock by impregnation with 14C-polymethylmethacrylate. *Journal of Contaminant Hydrology*, *13*(1-4), 403-418.

[13] Hong, S., Liu, P., Zhang, J., Xing, F., & Dong, B. (2019). Visual & quantitative identification of cracking in mortar subjected to

loads using X-ray computed tomography method. *Cement and Concrete Composites*, *100*, 15-24.

[14] Bay, B. K., Smith, T. S., Fyhrie, D. P., & Saad, M. (1999). Digital volume correlation: three-dimensional strain mapping using X-ray tomography. *Experimental mechanics*, *39*, 217-226.

[15] Valle, V., Bokam, P., Germaneau, A., & Hedan, S. (2019). New development of digital volume correlation for the study of fractured materials. *Experimental Mechanics*, *59*, 1-15.

[16] Bonnet, M., Sardini, P., Billon, S., Siitari-Kauppi, M., Kuva, J., Fonteneau, L., & Caner, L. (2020). Determining crack aperture distribution in rocks using the 14C-PMMA autoradiographic method: Experiments and simulations. *Journal of Geophysical Research: Solid Earth*, *125*(1), e2019JB018241.

[17] Bonnet, M., Caner, L., Siitari-Kauppi, M., Mazurier, A., Mexias, A. S., Dani, N., & Sardini, P. (2023). Weathering of Viamão granodiorite, south Brazil: Part 2–Initial porosity of un-weathered rock controls porosity development in the critical zone. *Geoderma*, *429*, 116247.

[18] Sardini, P., Ledésert, B., & Touchard, G. (1997). Quantification of microscopic porous networks by image analysis and measurements of permeability in the Soultz-sous-Forêts granite (Alsace, France). In *Fluid Flow and Transport in Rocks: Mechanisms and Effects* (pp. 171-189). Dordrecht: Springer Netherlands.

[19] Delayre, C., Mas, P. P., Sardini, P., Cosenza, P., & Thomas, A. (2020). Quantitative evolution of the petrophysical properties of andesites affected by argillic alteration in the hydrothermal system of Petite Anse-Diamant, Martinique. *Journal of Volcanology and Geothermal Research*, *401*, 106927.

[20] Loosveldt, H., Lafhaj, Z., & Skoczylas, F. (2002). Experimental study of gas and liquid permeability of a mortar. *Cement and concrete research*, *32*(9), 1357-1363.

[21] Goldstein, J. I., Newbury, D. E., Michael, J. R., Ritchie, N. W., Scott, J. H. J., & Joy, D. C. (2017). *Scanning electron microscopy and X-ray microanalysis*. springer.

[22] Soille, P. (1999). *Morphological image analysis: principles and applications* (Vol. 2, No. 3, pp. 170-171). Berlin: Springer.

[23] Schindelin, J., Arganda-Carreras, I., Frise, E., Kaynig, V., Longair, M., Pietzsch, T., ... & Cardona, A. (2012). Fiji: an open-source platform for biological-image analysis. *Nature methods*, *9*(7), 676-682.

[24] Ferreira, T., Rasband, W. ImageJ User Guide. https://imagej.nih.gov/ij/docs/guide/

[25] Valle, V., Bokam, P., Germaneau, A., & Hedan, S. (2019). New development of digital volume correlation for the study of fractured materials. *Experimental Mechanics*, *59*, 1-15.

[26] Valle, V., Hedan, S., Cosenza, P., Fauchille, A. L., & Berdjane, M. (2015). Digital image correlation development for the study of materials including multiple crossing cracks. *Experimental Mechanics*, *55*, 379-391.

[27] Allais, L., Bornert, M., Bretheau, T., & Caldemaison, D. (1994). Experimental characterization of the local strain field in a heterogeneous elastoplastic material. *Acta Metallurgica et materialia*, *42*(11), 3865-3880.

[28] Hedan, S., Valle, V., & Cosenza, P. (2020). Subpixel precision of crack lip movements by Heaviside-based digital image correlation for a mixed-mode fracture. *Strain*, *56*(6), e12346.

[29] Siitari-Kauppi, M. (2002). Development of 14C-polymethylmethacrylate method for the characterisation of low porosity media: Application to rocks in geological barriers of nuclear waste storage.

[30] Sardini, P., Siitari-Kauppi, M., Beaufort, D., & Hellmuth, K. H. (2006). On the connected porosity of mineral aggregates in crystalline rocks. *American Mineralogist*, *91*(7), 1069-1080.

[31] Sardini, P., El Albani, A., Pret, D., Gaboreau, S., Siitari-Kauppi, M., & Beaufort, D. (2009). Mapping and quantifying the clay aggregate microporosity in medium-to coarse-grained sandstones using the 14C-PMMA method. *Journal of Sedimentary Research*, *79*(8), 584-592.

[32] Sammaljärvi, J., Jokelainen, L., Ikonen, J., & Siitari-Kauppi, M. (2012). Free radical polymerisation of MMA with thermal initiator in brick and Grimsel granodiorite. *Engineering Geology*, *135*, 52-59.

[33] Keller, F., & Waser, P. G. (1982). Quantification in macroscopic autoradiography with Carbon-14—An evaluation of the method. *The International Journal of Applied Radiation and Isotopes*, *33*(12), 1427-1432.

[34] Mighani, S., Sondergeld, C. H., & Rai, C. S. (2016). Observations of tensile fracturing of anisotropic rocks. *Spe Journal*, *21*(04), 1289-1301.

[35] Buckman, J. (2014). Use of automated image acquisition and stitching in scanning electron microscopy: Imaging of large scale areas of materials at high resolution. *Microsc. Anal*, *28*(1), 13-15.

[36] Keller, A. (1998). High resolution, non-destructive measurement and characterization of fracture apertures. *International Journal of Rock Mechanics and Mining Sciences*, *35*(8), 1037-1050.

[37] Ketcham, R. A., Slottke, D. T., & Sharp Jr, J. M. (2010). Three-dimensional measurement of fractures in heterogeneous materials using high-resolution X-ray computed tomography. *Geosphere*, *6*(5), 499-514.

[38] Watanabe, N., Ishibashi, T., Ohsaki, Y., Tsuchiya, Y., Tamagawa, T., Hirano, N., ... & Tsuchiya, N. (2011). X-ray CT based numerical analysis of fracture flow for core samples under various confining pressures. *Engineering Geology*, *123*(4), 338-346.

[39] Reinhardt, M., Jacob, A., Sadeghnejad, S., Cappuccio, F., Arnold, P., Frank, S., ... & Kersten, M. (2022). Benchmarking conventional and machine learning segmentation techniques for digital rock physics analysis of fractured rocks. *Environmental Earth Sciences*, *81*(3), 71.

[40] Bodin, J., Delay, F., & de Marsily, G. (2003). Solute transport in a single fracture with negligible matrix permeability: 1. fundamental mechanisms. *Hydrogeology journal*, *11*, 418-433.